



HAL
open science

The effects of spatially distributed ionization sources on the temperature structure of HII regions

Barbara Ercolano, Nate Bastian, Grazyna Stasinska

► **To cite this version:**

Barbara Ercolano, Nate Bastian, Grazyna Stasinska. The effects of spatially distributed ionization sources on the temperature structure of HII regions. *Monthly Notices of the Royal Astronomical Society*, 2007, 379, pp.945-955. 10.1111/j.1365-2966.2007.12002.x . hal-03732878

HAL Id: hal-03732878

<https://hal.science/hal-03732878>

Submitted on 8 Sep 2022

HAL is a multi-disciplinary open access archive for the deposit and dissemination of scientific research documents, whether they are published or not. The documents may come from teaching and research institutions in France or abroad, or from public or private research centers.

L'archive ouverte pluridisciplinaire **HAL**, est destinée au dépôt et à la diffusion de documents scientifiques de niveau recherche, publiés ou non, émanant des établissements d'enseignement et de recherche français ou étrangers, des laboratoires publics ou privés.

The effects of spatially distributed ionization sources on the temperature structure of H II regions

B. Ercolano,^{1,2*} N. Bastian² and G. Stasińska³

¹Harvard-Smithsonian Centre for Astrophysics, 60 Garden Street, Cambridge, MA 02138, USA

²Department of Physics and Astronomy, University College London, Gower Street, London WC1E 6BT

³LUTH, Observatoire de Paris, CNRS, Université Paris Diderot; Place Jules Janssen 92190 Meudon, France

Accepted 2007 May 17. Received 2007 May 17; in original form 2007 April 4

ABSTRACT

Spatially resolved studies of star-forming regions show that the assumption of spherical geometry is not realistic in most cases, with a major complication posed by the gas being ionized by multiple non-centrally located stars or star clusters. Geometrical effects including the spatial configuration of ionizing sources affect the temperature and ionization structure of these regions. We try to isolate the effects of multiple non-centrally located stars via the construction of 3D photoionization models using the 3D Monte Carlo photoionization code MOCASSIN with very simple gas density distributions, but various spatial configurations for the ionization sources. Our first aim is to study the resulting temperature structure of the gas and investigate the behaviour of temperature fluctuations within the ionized region. We show that geometry affects the temperature structures in our models differently according to metallicity. For the geometries and stellar populations considered in our study, at intermediate and high metallicities, models with ionizing sources distributed in the full volume, whose Strömgren spheres rarely overlap, show *smaller* temperature fluctuation than their central ionization counterparts, with fully overlapping concentric Strömgren spheres. The reverse is true at low metallicities. Finally, the true temperature *fluctuations* due to the stellar distribution (as opposed to the large-scale temperature gradients due to other gas properties) are small in all cases and not a significant cause of error in metallicity studies.

Emission-line spectra from H II regions are often used to study the metallicity of star-forming regions, as well as providing a constraint for temperatures and luminosities of the ionizing sources. Empirical metallicity diagnostics must often be calibrated with the aid of photoionization models. However, most studies so far have been carried out by assuming spherical or plane-parallel geometries, with major limitations on allowed gas and dust density distributions and with the spatial distribution of multiple, non-centrally located ionizing sources not being accounted for. We compare integrated emission-line spectra from our models and quantify any systematic errors caused by the simplifying assumption of a single, central location for all ionizing sources. We find that the dependence of the metallicity indicators on the ionization parameter causes a clear bias due to the fact that models with a fully distributed configuration of stars always display lower ionization parameters than their fully concentrated counterparts. The errors found imply that the geometrical distribution of ionization sources may partly account for the large scatter in metallicities derived using model-calibrated empirical methods.

Key words: radiative transfer – H II regions – galaxies: abundances.

1 INTRODUCTION

The ability to measure accurate chemical abundances in H II regions in our own and other galaxies is vital for our understanding of

their chemical evolution. Emission lines emitted by the nebular gas photoionized by massive stars provide us with powerful metallicity indicators for near and intermediate redshift galaxies. The major complication is posed by the critical task of determining the physical parameters of the nebula, in particular the electron temperature, T_e . Failure to achieve realistic estimates may lead to gross errors in the final abundance determination. Temperature fluctuations within

*E-mail: bercolano@head.cfa.harvard.edu

the nebula may be an important cause of error. Collisionally excited lines (CELs), which are routinely used in abundance studies, are naturally weighted towards hotter regions and may therefore lead to underestimating of the real abundances. Recombination lines (RLs) are less affected by errors in temperature determinations, and should in theory yield more accurate results. One of the outstanding problems in nebular astrophysics is the discrepancy between abundances and electron temperature estimates obtained from CELs or RLs in Planetary Nebulae (PNe; see e.g. Rubin et al. 2002; Ercolano, Barlow & Storey 2005; Wesson, Liu & Barlow 2005; Liu et al. 2006; Peimbert & Peimbert 2006, and references therein), galactic and Magellanic H II regions (e.g. Peimbert, Peimbert & Ruiz 2000; Peimbert 2003; Tsamis et al. 2003; Esteban et al. 2004; García-Rojas et al. 2005, 2006) and extragalactic H II regions (e.g. Peimbert & Peimbert 2003; Peimbert, Peimbert & Ruiz 2005). The cause of this discrepancy is still uncertain; temperature fluctuations and chemical inhomogeneities in the gas have both been advocated to explain the discrepancy. Photoionization models including chemical inhomogeneities have been successful in matching the observed CEL and RL spectra of some PNe (e.g. Ercolano et al. 2003b) and H II regions (Tsamis & Péquignot 2005). However, the discrepancy between the abundances derived from RLs and those derived from CELs has also been attributed to temperature fluctuations *not* caused by abundance inhomogeneities (e.g. García-Rojas et al. 2004). The t^2 parameter (Peimbert 1967; Peimbert & Costero 1969; Peimbert 1971), introduced in order to quantify such fluctuations, can be derived empirically by the comparison of temperatures obtained from the depth of the Balmer jump to those obtained from CELs. Although the situation for H II regions is notoriously less worrying than for PNe, the problem still remains that empirically determined t^2 values are larger than those indicated by chemically homogeneous photoionization models, indicating that the causes of the proposed temperature fluctuations are still not understood.

Aside from temperature fluctuations, the task of obtaining reliable abundance estimates from CEL spectra of H II regions is further complicated by the fact that often the complete set of emission lines needed for a direct measurement of the electron temperatures is not available for all sources; the 4363 Å line of [O III] and the 5755 Å line of [N II] are weak and therefore not detected if the spectra do not have good signal-to-noise ratio or if the metallicities are high, implying low electron temperatures. A large effort has been made to provide metallicity and temperature indicators based on various combinations of strong lines (e.g. Alloin et al. 1979; Pagel et al. 1979; McGaugh 1991; Storchi-Bergmann, Calzetti & Kinney 1994; Vílchez & Esteban 1996; van Zee et al. 1998; Pilyugin 2001a; Pettini & Pagel 2004; Pérez-Montero & Díaz 2005). Hägele et al. (2006) have recently proposed a new methodology for the production and calibration of empirical relations between the different line temperatures based on observational data alone. However, the data sets available are still too limited to provide usable indicators. Currently, calibrations of metallicity indicators and ionic temperature relations are generally not based on observational data alone, but make use of grids of photoionization models, run for a range of metallicities and ionization parameters (e.g. McGaugh 1991; Charlot & Longhetti 2001; Kewley & Dopita 2002). Given the vast parameter space generally under investigation, most studies so far have been carried out with spherically symmetric or plane-parallel geometries, with major limitations on the allowed density distribution and with the spatial distribution of the ionizing sources not being investigated. Nearby H II regions, however, show complex structures in the distribution of gas and stars, which are often intermixed.

In this paper, we carry out a theoretical investigation of the importance of the effects due to the spatial distribution of the ionizing sources via the construction of a number of 3D photoionization models, using the MOCASSIN code (Ercolano et al. 2003a, 2005) for simple gas density distributions and three spatial configurations for the ionization sources.

Our modelling strategy is described in Section 2. Temperature fluctuations are estimated for our models by computing theoretical t^2 and T_0 values (Peimbert 1967) for each of our models, and the results are given and discussed in Section 3. In this section, we also compare integrated emission-line spectra from such configurations to search for systematic errors which may be caused by the simplifying assumption of a single, central location for all ionizing sources. We also test the robustness of a number of commonly used ionic temperature relations. A summary of our main results is presented in Section 4.

2 MODELLING STRATEGY

The aim of the current investigation is to uncover possible *systematic* differences on the temperature structure and emission-line spectra of nebulae ionized by a centrally concentrated set of stars or clusters versus those ionized by the same set of sources which are randomly distributed within the half or full volume, whose respective Strömgren spheres do or do not overlap. In particular, we want to test which of the stellar configurations considered produce the largest temperature fluctuations and of what magnitude. At this stage, we do not attempt to assess the absolute strengths and weaknesses of one metallicity indicator or ionic temperature relation over others, a task that may only be carried out by a systematic investigation of the large parameter space. In an attempt to isolate the effects of the stellar distribution from those due to the gas density distribution, we consider two extremely simple geometries – a homogeneous spherical volume and a homogeneous spherical shell, both of constant hydrogen number density, $N_{\text{H}} = 100 \text{ cm}^{-3}$. The shell models have inner radii of $2.8 \times 10^{19} \text{ cm}$ and Strömgren radii (corresponding to the case when all stars are located at the centre) as listed in Table 1. The total number of ionizing photons is constant for all models and is $Q_{\text{H}^0} = 3.80 \times 10^{50} \text{ s}^{-1}$.

For each density distribution, we are interested in a comparison between the centrally concentrated and the half and fully distributed source cases. In the remainder of this paper, we will refer to models ionized by a central concentration of stars as Models C, and those

Table 1. Characterizing model parameters. L_{bol} is the total bolometric luminosity of all stars included. R_{s} is the Strömgren radius in the case when all stars are located at the centre of the sphere/shell. The total number of ionizing photons and the hydrogen number density are constant for all models and are, respectively, $Q_{\text{H}^0} = 3.80 \times 10^{50} \text{ s}^{-1}$ and $N_{\text{H}} = 100 \text{ cm}^{-3}$. All shell models have an inner radius of $2.8 \times 10^{19} \text{ cm}$.

Z/Z_{\odot}	L_{bol} [E40 erg s $^{-1}$]	R_{s} [E19 cm]	
		Sphere	Shell
2.0	3.30	2.65	3.45
1.0	3.00	2.85	3.55
0.4	2.64	3.20	3.75
0.2	2.30	3.45	3.90
0.05	1.98	3.75	4.20

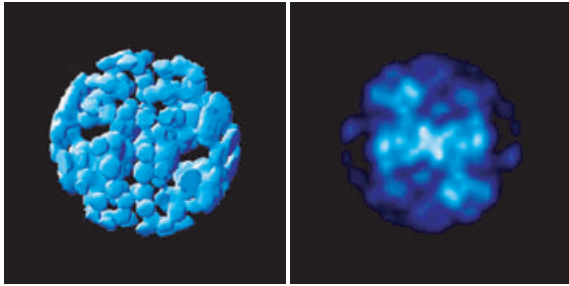


Figure 1. The left-hand panel shows a 3D representation of the Strömgren sphere distribution for Case F, plotted as the iso-surfaces where the ionization fraction of hydrogen is 0.95. The adjacent right-hand panel shows an average projection map of the ionic abundance of H^+ .

ionized by the same set of stars distributed in the half and full volumes will be referred to as Models H and F, respectively. Case C is equivalent to models ionized by a single central source with a total bolometric luminosity equal to the sum of the bolometric luminosities of the individual sources (as given in Table 1) and a spectral shape given by the superposition of the spectra of all sources. These models could also be performed using a 1D code, with a spherically symmetric gas density distribution. Similarly, a 1D code could also be employed for Case F models where the Strömgren spheres do not generally overlap;¹ the left-hand panel of Fig. 1 shows a 3D representation of the Strömgren sphere distribution for Case F, plotted as iso-surfaces where the ionization fraction of hydrogen is 0.95. The adjacent panel shows a projected map of the ionic abundance of H^+ . In the intermediate case, Case H, the Strömgren spheres of most H II regions partially overlap; the determination of the radiation field in the overlap region is not possible without the application of a 3D code. As we are interested in a comparison of the three cases (C, H and F), self-consistency is crucial and for this reason we have run all models with the same 3D code, MOCASSIN.

Our models include five metallicities ($Z/Z_{\odot} = 0.05, 0.2, 0.4, 1.0, 2.0$). The ‘solar’ abundance set uses the values from Grevesse & Sauval (1998) with the exception of C, N, O abundances which are taken from Allende Prieto et al. (2002), Holweger (2001) and Allende Prieto, Lambert & Asplund (2001), respectively. These were scaled to lower and higher metallicities considering the empirical abundance trends observed in H II regions by Izotov et al. (2006). In order to maximize the effects of spatially distributed sources whose Strömgren spheres may overlap (completely or partially), or be totally independent, we consider the limiting case of an ionizing set composed of two stellar populations, a 37 and a 56 M_{\odot} population, with half of the total ionizing photon output (s^{-1}) being emitted by each population. These two stellar masses were chosen as they have very different Q_{He^0}/Q_{H^0} ratios, where Q_{H^0} is the total output [s^{-1}] of H-ionizing photons (energy > 1 ryd) and Q_{He^0} is the total output [s^{-1}] of He-ionizing photons (energy > 1.8 ryd), and are likely to produce the largest effects on the temperature structure and sharpness of the ionization front. The ionizing spectra for single-mass stars were computed with the STARBURST99 spectral synthesis code (Leitherer et al. 1999) with the up-to-date non-LTE stellar atmospheres implemented by Smith, Norris & Crowther (2002) using single isochrones for the appropriate stellar masses. The models

¹ Due to the stochastic nature of the ionization source distribution, it is possible that a small fraction of them may actually have partially overlapping Strömgren spheres.

were calculated at metallicities consistent with the nebular gas and were obtained for an instantaneous burst at an age of 1 Myr. At solar metallicities for the 37 M_{\odot} stars, the stellar atmosphere models emit 32.3 per cent of luminosity in the H-ionizing continuum and 7.7 per cent in the He-ionizing continuum, while for the 56 M_{\odot} stars these percentages are 47.9 and 13.7 per cent, respectively. The exact percentages vary with stellar metallicity, nevertheless the values above are given as a guide to appreciate the different spectral hardness of the two populations.

Some other defining parameters of our models, together with their nomenclature and associated symbols, are given in Table 2.

2.1 The 3D photoionization code: MOCASSIN

The 3D photoionization code MOCASSIN (Ercolano et al. 2003a, 2005) uses a Monte Carlo approach to the radiation transport problem and it is therefore completely independent of geometry and density distribution. Both the stellar and diffuse components of the radiation field are treated self-consistently, without the need of approximations. Multiple ionization sources can be located at arbitrary positions in the simulation grid with the only limit being imposed by computing resources. The atomic data used are frequently updated and include sets of energy levels, collision strengths and transition probabilities from Version 5 of the Chianti data base (Landi et al. 2005) and the improved H I, He I and He II free-bound continuous emission data recently published by Ercolano & Storey (2006). A public version of the FORTRAN 90 code, which is fully parallelized using the Message Passing Interface (MPI) libraries, can be obtained from B. Ercolano. Version 2.02.38 was used for the models presented in this work. We simulate one quadrant of each model, using the technique described and tested by Ercolano et al. (2003b), whereby the positive x - y , y - z and x - z planes intersecting the z -, x - and y -axes, respectively, at zero act as mirrors, reflecting the incoming photons back into the simulated cube. The full volume is finally described by 10^6 cells for the shell models and by 125 000 cells for the spherical models ionized by 240 sources. The number of energy packets used varies during the course of our simulations, but typically 1–10 million packets are sufficient for our grids to reach convergence within 10–20 iterations. We experimented with higher-resolution grids and a larger number of energy packets and found our results to be virtually unaffected.

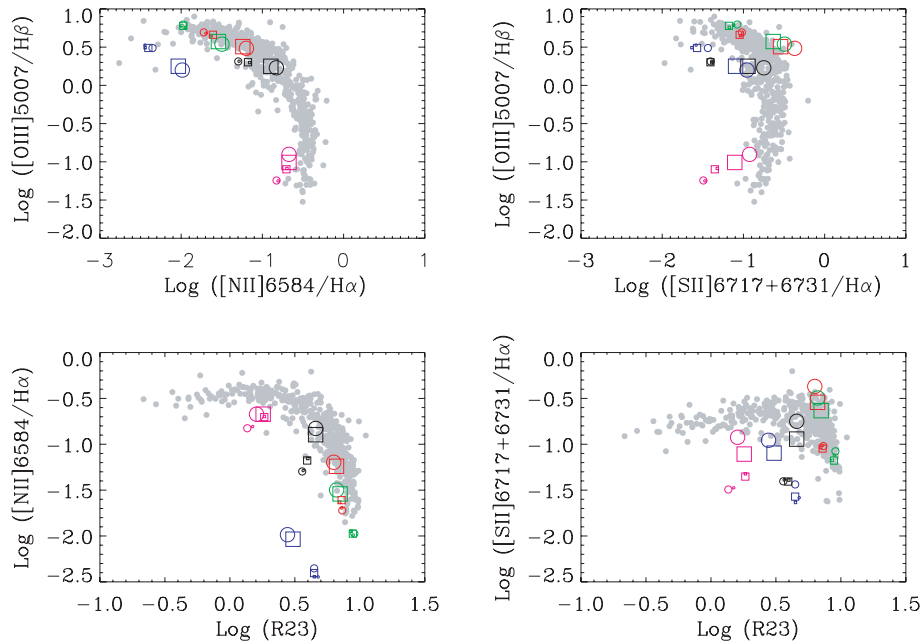
2.2 Validation of our models

As stated above, the aim of this paper is not to provide new calibrations to abundance diagnostic ratios or to assess their absolute accuracy. It is therefore not our intention to create models that fit any particular observations. While trying to maximize the effects of a complex ionizing field distribution, it is, however, still necessary to ensure that the ionization and temperature structures and, hence, emission-line ratios we obtain from our models are in the range of those observed in nature. In Fig. 2, we plot our results in a number of line ratio diagrams, including those following Veilleux & Osterbrock (1987) and Osterbrock, Tran & Veilleux (1992), that show the variation in [N II] and [S II] excitation parametrized in terms of [O III]/ $H\beta$ (top panels) and those following McCall, Rybski & Shields (1985) showing the variation in terms of R23.² Similarly, in Fig. 3 we plot the H II region ionization sequence parametrized

² $R23 = ([O III] 5007,4959 + [O II] 3726,3729)/H\beta$.

Table 2. Model grid legend. H number density, $N_{\text{H}} = 100 [\text{cm}^{-3}]$ for all models. Figures in this paper rely on colour, please refer to online version. For black and white copies black is black, blue is dark-grey, red is medium grey and green is light grey.

Model	Star distrib.	Geometry	Z/Z_{\odot}	Symbol	Model	Star distrib.	Geometry	Z/Z_{\odot}	Symbol
CSp2.0	Central	Sphere	2.0	Small magenta circle	CSh0.4	Central	Shell	0.4	Small red square
HSp2.0	Half distrib	Sphere	2.0	Medium magenta circle	HSh0.4	Half distrib	Shell	0.4	Medium red square
FSp2.0	Fully distrib	Sphere	2.0	Large magenta circle	FSh0.4	Fully distrib	Shell	0.4	Large red square
CSh2.0	Central	Shell	2.0	Small magenta square	CSp0.2	Central	Sphere	0.2	Small green circle
HSh2.0	Half distrib	Shell	2.0	Medium magenta square	HSp0.2	Half distrib	Sphere	0.2	Medium green circle
FSh2.0	Fully distrib	Shell	2.0	Large magenta square	FSp0.2	Fully distrib	Sphere	0.2	Large green circle
CSp1.0	Central	Sphere	1.0	Small black circle	CSh0.2	Central	Shell	0.2	Small green square
HSp1.0	Half distrib	Sphere	1.0	Medium black circle	HSh0.2	Half distrib	Shell	0.2	Medium green square
FSp1.0	Fully distrib	Sphere	1.0	Large black circle	FSh0.2	Fully distrib	Shell	0.2	Large green square
CSh1.0	Central	Shell	1.0	Small black square	CSp0.05	Central	Sphere	0.05	Small blue circle
HSh1.0	Half distrib	Shell	1.0	Medium black square	HSp0.05	Half distrib	Sphere	0.05	Medium blue circle
FSh1.0	Fully distrib	Shell	1.0	Large black square	FSp0.05	Fully distrib	Sphere	0.05	Large blue circle
CSp0.4	Central	Sphere	0.4	Small red circle	CSh0.05	Central	Shell	0.05	Small blue square
HSp0.4	Half distrib	Sphere	0.4	Medium red circle	HSh0.05	Half distrib	Shell	0.05	Medium blue square
FSp0.4	Fully distrib	Sphere	0.4	Large red circle	FSh0.05	Fully distrib	Shell	0.05	Large blue square

**Figure 2.** H II region excitation sequence in terms of $[\text{N II}]/\text{H}\alpha$ and $[\text{S II}]/\text{H}\alpha$ versus $[\text{O III}]/\text{H}\beta$ and R23. The grey points represent giant H II regions in galaxies taken from Garnett & Kennicutt (1994), Garnett et al. (1997), van Zee et al. (1998), Bresolin et al. (1999, 2004, 2005) and Kennicutt, Bresolin & Garnett (2003), spanning metallicities from $12 + \log(\text{O}/\text{H}) \sim 8$ to ~ 8.8 , and metal-poor emission-line galaxies from Izotov et al. (2006), which extend to $12 + \log(\text{O}/\text{H}) \sim 7.2$. The symbols and colours correspond to our models as defined in Table 2. (Please refer to the online version of this paper for colour figures.)

in terms of oxygen and sulphur line ratios.³ The grey dots represent giant H II regions in spiral galaxies, taken from Garnett & Kennicutt (1994), Garnett et al. (1997), van Zee et al. (1998), Bresolin, Kennicutt & Garnett (1999), Bresolin, Garnett & Kennicutt (2004), Bresolin et al. (2005) and Kennicutt et al. (2003), spanning metallicities from $12 + \log(\text{O}/\text{H}) \sim 8$ to ~ 8.8 . Fig. 2 and the top right panel of Fig. 3 also include a few points from metal-poor emission-

line galaxies from Izotov et al. (2006), which extend to $12 + \log(\text{O}/\text{H}) \sim 7.2$; it was not possible to use these data for the other three panels of Fig. 3 due to the lack of simultaneous detection of all the oxygen and sulphur lines needed. In general, our models fall within or near the locus of observed H II regions, with the exception of our lowest metallicity ($Z/Z_{\odot} = 0.05$) and highest metallicity ($Z/Z_{\odot} = 2$) models, which is not surprising given that the observational sets available did not include many data points at such extreme values of Z ; furthermore we did not attempt any systematic variation of the ionization parameter with Z , while observations of giant H II regions argue that the ionization parameter decreases as Z

³ $\eta' = ([\text{O II}] 3726, 3729 / [\text{O III}] 5007, 4959) / ([\text{S II}] 6716, 6731 / [\text{S III}] 9069, 9532)$.

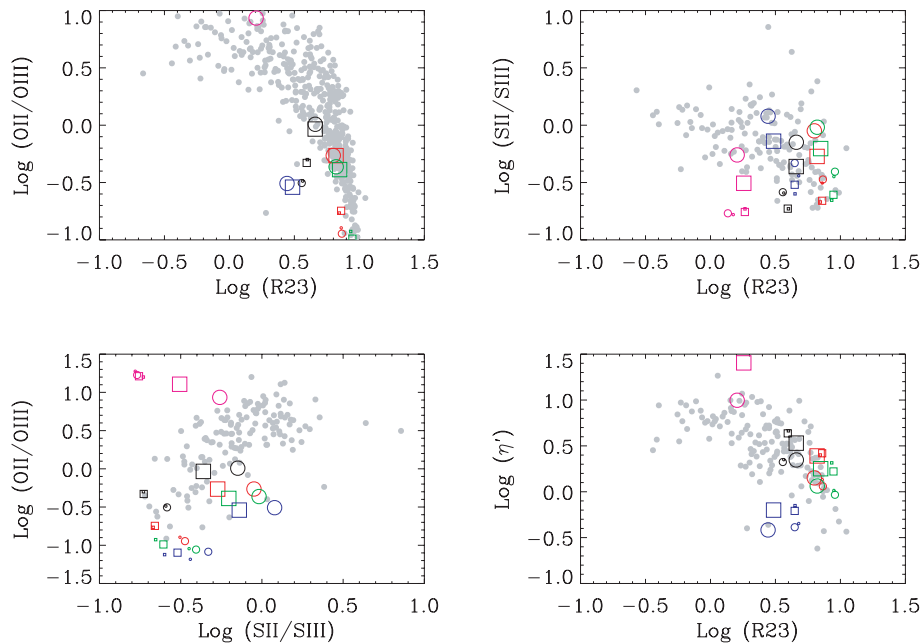


Figure 3. H II region ionization sequence parametrized in terms of oxygen and sulphur. The grey dots indicate the position of giant H II regions in spiral galaxies taken from Garnett & Kennicutt (1994), Garnett et al. (1997), van Zee et al. (1998), Bresolin et al. (1999, 2004, 2005), Kennicutt et al. (2003), spanning metallicities from $12 + \log(\text{O}/\text{H}) \sim 8$ to ~ 8.8 . The top right panel also includes a few points from metal-poor emission-line galaxies from Izotov et al. (2006), which extend to $12 + \log(\text{O}/\text{H}) \sim 7.2$; it was not possible to use these data for the other three panels due to the lack of simultaneous detection of all the lines needed. The symbols and colours correspond to our models as defined in Table 2. (Please refer to the online version of this paper for colour figures.)

increases (see e.g. McGaugh 1994). However, this does not affect the achievement of our aims.

3 RESULTS

The temperature structure and emission-line spectra obtained by our models are analysed here in detail. Temperature fluctuations, which may introduce errors in the empirical calculations of abundances, are examined. The robustness of commonly used abundance diagnostics and ionic temperature relations are also tested against possible errors introduced by geometrical effects.

3.1 Temperature structure

The volume-integrated electron temperatures weighted by a number of commonly observed ionic species are plotted in Fig. 4 for metallicities of $Z/Z_{\odot} = 0.05, 0.2, 0.4, 1$ and 2 . The values were obtained according to

$$T_e(\text{X}^{+i}) = \frac{\int N_e N(\text{X}^{+i}) T_e dV}{\int N_e N(\text{X}^{+i}) dV}. \quad (1)$$

The models are represented by circles and squares of various colours and sizes as described in Table 2.

At a first glance some trends are apparent. At solar and high metallicities (i.e. $Z/Z_{\odot} \geq 1$), the electron temperatures in ‘high’ ionic species zones (e.g. O III, S III, Ar III and N III) are higher for models in Cases H and F. The opposite is true for electron temperatures in ‘low’ ionic species zones, such as O II and N II. This implies a shallower temperature gradient for Cases F and H when compared to Case C, since at these metallicities the highest nebular temperatures are reached in the low-ionization zones which are not affected by the very efficient cooling provided by the infrared (IR) fine-structure lines of [O III] as in the high-ionization zones,

where, in fact, the lowest temperatures are reached. The $Z/Z_{\odot} = 0.05$ and 0.2 models do not follow the same trend; here there is a monotonic shift of temperatures, whereby C models are hotter than the H and F models, regardless of ionic species zone. At intermediate metallicities ($Z/Z_{\odot} = 0.4$), we are in a transition case from the two separate behaviours described above. At low metallicities, the cooling is dominated by collisional excitation of H Ly α , which increases as one gets closer to the ionization front, where the proportion of residual neutral hydrogen increases. This results in an outward decreasing temperature, contrary to the high-metallicity cases.

Differences in the temperature structure of Cases F and C can be understood as follows: at each point in the nebula the electron temperature is primarily determined by the average energy of the photons absorbed by H and He and by the cooling efficiency of the ions. The latter is naturally less important at lower metallicities. However, for the intermediate- to high-metallicity cases, it is differences in the distribution of the cooling ions rather than differences in the heating rates which explain the difference in temperature structure between Cases C and H for higher and intermediate metallicities.

3.2 Temperature fluctuations

We have calculated for the main ionic species in our models the formal values of the mean ionic temperatures, T_0 , and of the temperature fluctuations, t^2 , according to the formalism of Peimbert (1967). Note that in the case of concentric sources, t^2 measures changes in radial gradients of the temperature rather than ‘temperature fluctuations’ while in the cases of distributed sources it really represent a temperature fluctuation. For brevity, we only list the values for H⁺, O⁺ and O²⁺ in Table 3. The errors quoted in the table are representative of the accuracy achieved by our models. They contain contributions from the variance intrinsic to our Monte Carlo approach and the

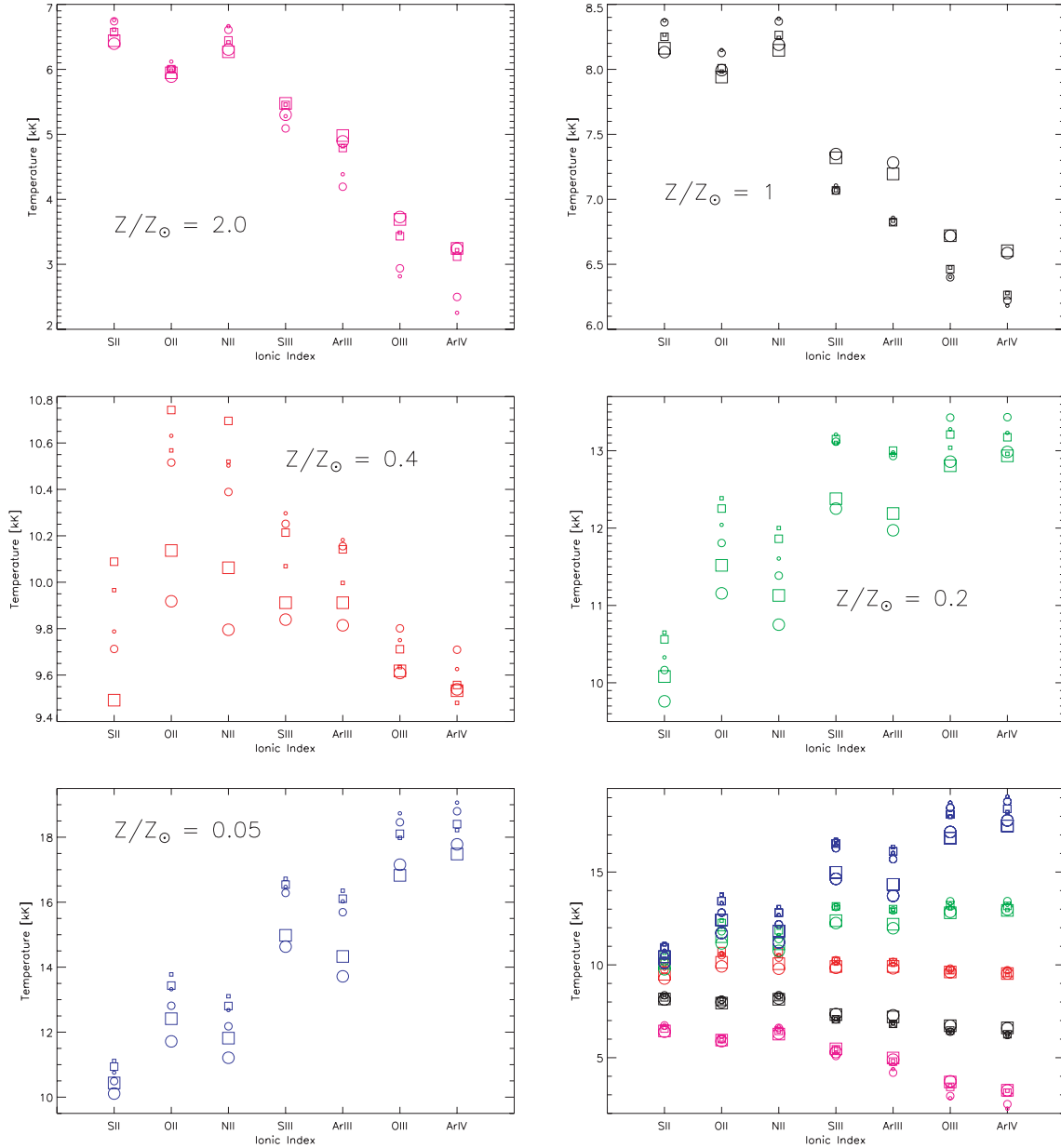


Figure 4. Volume-integrated electron temperatures weighted by ionic species. Top left: results for all models with $Z/Z_{\odot} = 2$ (magenta); top right: results for all models at $Z/Z_{\odot} = 1$ (black); middle left: results for all models at $Z/Z_{\odot} = 0.4$ (red); middle right: results for all models at $Z/Z_{\odot} = 0.2$ (green); bottom left: results for all models at $Z/Z_{\odot} = 0.05$ (blue); bottom right: results for all models at all metallicities. A legend for the symbols is given in Table 2. (Please refer to the online version of this paper for colour figures.)

error introduced by using a finite grid to describe the ionized region. The errors were estimated by considering that for a fully spherically symmetric case, such as one with homogeneous gas density distribution and a central location for all ionizing sources, the t^2 in an infinitely narrow spherical shell centred on the source of the ionizing photons should be zero. We note that our errors increase with increasing metallicities, this is due to the larger temperature gradients occurring at higher metallicities causing the error contribution due to the finite grid description to increase. Clearly, all errors could be reduced by increasing the number of energy packets and grid cells used in the simulations. However, we note that our errors are always at least one order of magnitude smaller than the t^2 values and therefore do not affect our conclusions. Given the large number of 3D models run for this work (which vastly exceeds those finally

presented here), we feel that a good balance between accuracy and computational expense was achieved.

The value of $t^2(\text{O}^+)$ is very hard to derive empirically. We know, however, of three H II regions where this measurement has been made: the Orion nebula (Esteban et al. 2004), M20 (García-Rojas et al. 2006) and M8 (García-Rojas et al. 2007). In those cases where $t^2(\text{O}^+)$ cannot be derived empirically, it is generally assumed that $t^2(\text{O}^+) = t^2(\text{O}^{2+})$; it is clear from the values listed in our table that this assumption is very often not verified and care should be taken to account for this in the error estimation from such studies. For our $Z/Z_{\odot} = 2$ models, $t^2(\text{O}^{2+})$ is always a factor of 2 or more higher than $t^2(\text{O}^+)$, while for lower metallicities $t^2(\text{O}^{2+})$ becomes lower than $t^2(\text{O}^+)$ sometimes by large factors (up to approximately 10). Finally, we note that the formal t^2 values may diverge from the

Table 3. Mean temperatures and temperature fluctuations quantified in terms of $T_0(\text{H}^+)$, $t^2(\text{H}^+)$, $T_0(\text{O}^+)$, $t^2(\text{O}^+)$, $T_0(\text{O}^{2+})$ and $t^2(\text{O}^{2+})$ (Peimbert 1967).

Model	$T_0(\text{H}^+)$	$t^2(\text{H}^+)$	$T_0(\text{O}^+)$	$t^2(\text{O}^+)$	$T_0(\text{O}^{2+})$	$t^2(\text{O}^{2+})$
CSphH0.05	18240	0.0178	13350	0.041	18500	0.007
HSphH0.05	17690	0.0228	12830	0.046	18500	0.007
FSphH0.05	14850	0.0511	11720	0.035	17180	0.009
		± 0.0006		± 0.003		± 0.004
CSphH0.2	13140	0.0034	12060	0.0145	13430	0.0010
HSphH0.2	13230	0.0036	11810	0.0156	13430	0.0005
FSphH0.2	12100	0.0112	11160	0.0141	12860	0.0010
		± 0.0001		± 0.0004		± 0.0001
CSphH0.4	9850	0.0063	10620	0.0069	9790	0.0053
HSphH0.4	9860	0.0038	10500	0.0060	9790	0.0029
FSphH0.4	9710	0.0036	9910	0.0047	9600	0.0024
		± 0.0005		± 0.0007		± 0.0003
CSphH1.0	6690	0.024	8130	0.020	6380	0.012
HSphH1.0	6670	0.021	8110	0.020	6380	0.009
FSphH1.0	7320	0.018	7990	0.012	6710	0.009
		± 0.006		± 0.002		± 0.001
CSphH2.0	5000	0.156	6110	0.043	2910	0.130
HSphH2.0	4880	0.152	5980	0.050	2919	0.096
FSphH2.0	5360	0.075	5890	0.036	3700	0.084
		± 0.005		± 0.003		± 0.003
CShhH0.05	17510	0.0129	13770	0.0437	18110	0.0041
HShhH0.05	17520	0.0166	13440	0.0438	18110	0.0057
FShhH0.05	15200	0.0369	12410	0.0348	16840	0.0098
		± 0.0002		± 0.0002		± 0.0001
CShhH0.2	12940	0.0033	12390	0.0113	13210	0.0017
HShhH0.2	13080	0.0029	12250	0.0124	13210	0.0010
FShhH0.2	12280	0.0082	11520	0.0121	12810	0.0015
		± 0.0002		± 0.0002		± 0.0007
CShhH0.4	9780	0.0091	10570	0.0089	9710	0.0078
HShhH0.4	9880	0.0084	10740	0.0081	9710	0.0068
FShhH0.4	9810	0.0060	10130	0.0064	9620	0.0046
		± 0.0003		± 0.0003		± 0.0001
CShhH1.0	6880	0.030	7980	0.026	6460	0.017
HShhH1.0	6850	0.029	8010	0.026	6460	0.016
FShhH1.0	7280	0.021	7940	0.017	6720	0.012
		± 0.001		± 0.001		± 0.001
CShhH2.0	5450	0.086	5980	0.045	3420	0.09
HShhH2.0	5430	0.090	6000	0.045	3420	0.09
FShhH2.0	5490	0.070	5950	0.037	3690	0.08
		± 0.006		± 0.006		± 0.01

empirical ones (e.g. Kingdon & Ferland 1995; Zhang, Ercolano & Liu 2007) that are generally based on the comparison of the electron temperature derived from the depth of the Balmer jump and the [O III] temperature, the values listed in Table 3 are, nevertheless, sufficient to identify the effects of the stellar distribution on temperature fluctuations in the nebular gas.

In Fig. 5, we plot the t^2 values for H^+ and O^{2+} (dashed and solid lines, respectively) against metallicity for the spherical and shell models. Cases C, H and F are represented by black, red and green lines and symbols, respectively. Unsurprisingly, the temperature fluctuations, which in this case are a direct consequence of large-scale temperature gradients, are larger for the high-metallicity models. A full discussion of this effect and of the causes of the large-scale temperature fluctuations in metal-rich nebulae is given by Stasińska (1980) and Kingdon & Ferland (1995). What had not been noted before, however, is that at very low metallicities, the t^2 values for H^+ and O^+ rise again; this is due to the large temperature gradient already shown in Fig. 4. However, $t^2(\text{O}^{2+})$ remains tiny, so

that the overall effect on abundance determinations is expected to be small.

With regard to a comparison of the t^2 values obtained with the three different spatial distributions of sources (Cases C, H and F), we first of all note that for intermediate to high metallicities ($Z/Z_\odot \geq 0.4$), Case F models show a more isothermal gas (smaller t^2) than Case H or C models. This is due to the fact that the contributions to the t^2 due to the true temperature fluctuations created by the two different stellar populations in Case F (and in a smaller degree in Case H) are completely washed out by the large-scale temperature gradients caused by the metals' cooling. This effect vastly dominates at these metallicities, resulting in larger values of t^2 being obtained by Case C models, which, as discussed in the previous section (see Fig. 4), have steeper temperature gradients than their Case H and F counterparts.

The above is further confirmed by the fact for very low metallicities ($Z/Z_\odot \leq 0.2$), Case F models (green lines) show larger fluctuations than Case C and H models. This is because at these low metallicities, Cases C, H and F all show similar large-scale temperature gradients (see Fig. 4); the values of t^2 are thus larger for Case F models where true temperature fluctuations are at play. However, once again we point out that no large effects are expected on abundance determinations due to the fact that $t^2(\text{O}^{2+})$ is small in all cases.

3.3 Ionic temperature relations

We have shown that the temperature structure of models with centrally concentrated ionizing sources, Case C, may vary compared to those of similar models where the sources are distributed within the half volume (Case H), which have partially overlapping Strömgen spheres, and to those with sources distributed within the full volume (case F), which have fully independent Strömgen spheres. Case C to F variations in the temperature structure of the models may have implications for a number of ionic temperature relations. These scaling laws are often employed in abundance studies when observational data for a given ionic zone are missing. Some of the most popular relations we found in the literature include $T_e(\text{S III})$ versus $T_e(\text{Ar III})$, $T_e(\text{O III})$ versus $T_e(\text{Ar III})$ and $T_e(\text{O II})$ versus $T_e(\text{N II})$. These ratios are expected to be around unity and we found them to be very little affected by the shifts in temperatures due to the spatial distribution of stars. This is not surprising, given that the ionic species involved are both 'high' (O III, S III, Ar III and N III) or 'low' (O II and N II), and therefore while the absolute temperature values in each case may shift to higher or lower values, the resulting ratios remain virtually unaffected.

Scaling laws have also been derived for $T_e(\text{O III})$ versus $T_e(\text{S III})$ and $T_e(\text{O III})$ versus $T_e(\text{O II})$ by Garnett (1992), based on his own grids of photoionization models and those by Stasińska (1982). More recently, Izotov et al. (2006) produced somewhat different relations between $T_e(\text{O II})$ and $T_e(\text{O III})$, and between $T_e(\text{S III})$ and $T_e(\text{O II})$ [their equations 14 and 15, valid only for metal-poor cases to $12 + \log(\text{O}/\text{H}) \sim 8.2$], based on a set of up-to-date (but still spherically symmetric) photoionization models that reproduce the observed trends of metal-poor galaxies. They found that the observed values of $T_e(\text{O II})$, $T_e(\text{O III})$ and $T_e(\text{S III})$ in a large sample of H II galaxies reproduce the theoretical relations, but with a large scatter [not only attributable to observational errors in the case of $T_e(\text{O II})$, $T_e(\text{O III})$, see their figs 4a and b].

Fig. 6 shows the behaviour of our $Z/Z_\odot = 1.0$ and 2.0 (left-hand panel, black and magenta symbols, respectively) and $Z/Z_\odot = 0.05$, 0.2 and 0.4 (right-hand panel, blue, green and red symbols,

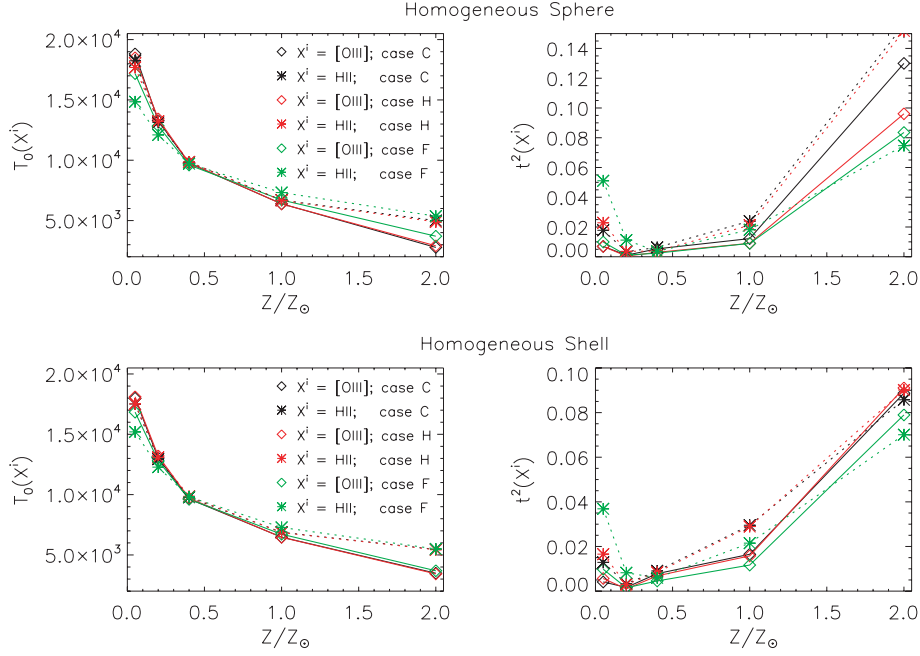


Figure 5. Mean ionic temperatures and temperature fluctuations as a function of gas metallicity for the homogeneous sphere and shell models. $T_0(\text{O}^{2+})$ and $T_0(\text{H}^+)$ are represented by solid and dashed lines, respectively. The lines are colour coded such that black, red and green are for Cases C, H and F, respectively. (Please refer to the online version of this paper for colour figures.)

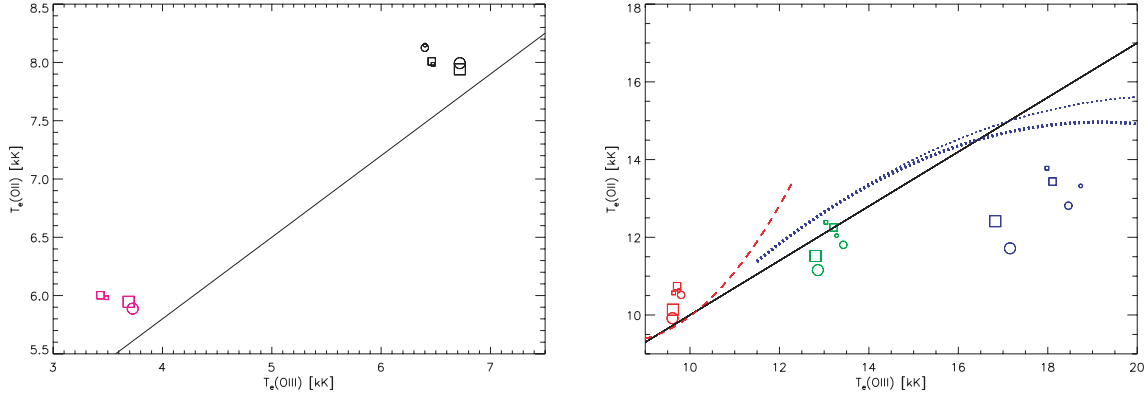


Figure 6. $T_e(\text{O II})$ versus $T_e(\text{O III})$ for $Z/Z_\odot = 1.0$ and 2.0 (left-hand side) and $Z/Z_\odot = 0.05, 0.2$ and 0.4 (right-hand side) models for Cases C, H and F. The straight black solid line is the scaling law of Garnett (1992) and the blue dotted and red dashed curves are the relations given in equation (14) of Izotov et al. (2006) for $12 + \log(\text{O}/\text{H}) = 8.2$ (red), 7.6 (blue dotted, thick) and 7.2 (blue dotted, thin). The symbols representing our models are described in Table 2. (Please refer to the online version of this paper for colour figures.)

respectively) metallicity models for Cases C, H and F with regard to the $T_e(\text{O II})$ versus $T_e(\text{O III})$ scaling laws of Garnett (1992, black solid line in both panels) and Izotov et al. (2006, coloured curves in the right-hand panels). The symbols are as described in Table 2. Our lowest metallicity bin $Z/Z_\odot = 0.05$ [corresponding to $12 + \log(\text{O}/\text{H}) = 7.39$] falls in between Izotov’s $12 + \log(\text{O}/\text{H}) = 7.2$ and 7.6 metallicity bins. Their $T_e(\text{O III})$ versus $T_e(\text{O II})$ relations given in their equation (14) are therefore plotted in blue in the right-hand panel of our Fig. 6, with the thinner and thicker curves indicating the 7.2 and 7.6 metallicity bin, respectively. Our $Z/Z_\odot = 0.4$ metallicity bin (red symbols) corresponds to $12 + \log(\text{O}/\text{H}) = 8.29$, slightly above Izotov’s $12 + \log(\text{O}/\text{H}) = 8.2$ bin which, nevertheless, is represented by the red line in Fig. 6.

A ‘mixed’ relation such as $T_e(\text{O III})$ versus $T_e(\text{O II})$ is much more affected by the fact that low and high ionic temperatures shift in

opposite directions for intermediate (red points; $Z/Z_\odot = 0.4$) and high metallicities (magenta and black points; $Z/Z_\odot = 2$ and 1). This will contribute to the scatter noted observationally for this relation. For example, Kennicutt et al. (2003) presented a study of those H II regions in M101 for which direct measurements of the nebular auroral lines could be obtained. They found the $T_e(\text{O III})$ versus $T_e(\text{S III})$ relation to be matched closely by their observations, whereas the $T_e(\text{O III})$ and $T_e(\text{O II})$ temperatures turned out to be rather uncorrelated. It is also worth noting at this point that another factor that could contribute to the scatter in the $T_e(\text{O III})$ versus $T_e(\text{O II})$ relation is the dependency of $T_e(\text{O II})$ on the electron density (Pérez-Montero & Díaz 2003). The scatter found by our models is for a given electron density, and therefore it may be even larger for a different sample covering a wider range of densities. The ionizing flux distribution is certainly a factor that contributes to weakening

Table 4. Oxygen abundances derived applying various metallicity indicators to the integrated emission-line spectra calculated for our models (see text for calibrations used). All abundances are given in logarithmic scale, $12 + \log(\text{O}/\text{H})$. The input values of $12 + \log(\text{O}/\text{H})$ (i.e. ‘the right answer’) are 8.99 ($Z/Z_{\odot} = 2$), 8.69 ($Z/Z_{\odot} = 1$), 8.29 ($Z/Z_{\odot} = 0.4$), 7.99 ($Z/Z_{\odot} = 0.2$) and 7.39 ($Z/Z_{\odot} = 0.05$). $|\Delta|$, the largest difference between the abundance derived from C, H and F cases is given for each model trio. The value averaged over all models, $\langle |\Delta| \rangle$, is given in the last row of the table.

Model	O ₂₃	O ₃ N ₂	N ₂	S ₂₃	S ₃ O ₃	Ar ₃ O ₃	Model	O ₂₃	O ₃ N ₂	N ₂	S ₂₃	S ₃ O ₃	Ar ₃ O ₃
CSp2.0	8.67	8.78	8.44	7.92	8.77	8.83	CSh2.0	8.62	8.77	8.50	8.09	8.75	8.82
HSp2.0	8.69	8.78	8.43	7.87	8.76	8.81	HSh2.0	8.62	8.77	8.50	8.08	8.75	8.82
FSp2.0	8.67	8.73	8.52	8.17	8.67	8.78	FSh2.0	8.63	8.76	8.52	8.16	8.72	8.81
$ \Delta $	0.02	0.05	0.09	0.30	0.10	0.05	$ \Delta $	0.01	0.01	0.02	0.08	0.03	0.01
CSp1.0	8.74	8.27	8.17	7.76	8.04	8.48	CSh1.0	8.66	8.30	8.24	7.94	8.16	8.55
HSp1.0	8.75	8.27	8.16	7.73	8.02	8.46	HSh1.0	8.67	8.30	8.23	7.92	8.14	8.54
FSp1.0	8.49	8.40	8.43	8.34	8.24	8.62	FSh1.0	8.51	8.38	8.39	8.23	8.24	8.61
$ \Delta $	0.26	0.13	0.27	0.61	0.22	0.16	$ \Delta $	0.16	0.08	0.16	0.31	0.10	0.07
CSp0.4	8.52	8.07	7.87	7.93	8.28	7.96	CSh0.4	8.52	8.09	7.97	8.49	8.10	7.77
HSp0.4	8.52	8.06	7.85	7.92	8.22	7.91	HSh0.4	8.50	8.10	7.98	8.45	8.08	7.73
FSp0.4	8.43	8.24	8.15	8.22	9.02	8.25	FSh0.4	8.41	8.23	8.19	8.92	8.27	8.12
$ \Delta $	0.09	0.18	0.30	0.30	0.80	0.34	$ \Delta $	0.11	0.14	0.22	0.47	0.19	0.39
CSp0.2	7.86	7.97	7.77	7.99	7.67	7.67	CSh0.2	7.84	7.99	7.79	8.18	7.87	7.92
HSp0.2	7.87	7.97	7.77	8.01	7.66	7.66	HSh0.2	7.86	7.97	7.77	8.10	7.79	7.82
FSp0.2	7.68	8.15	8.05	8.68	8.10	8.26	FSh0.2	7.72	8.13	8.02	8.61	8.11	8.26
$ \Delta $	0.19	0.18	0.28	0.69	0.44	0.60	$ \Delta $	0.14	0.16	0.25	0.51	0.32	0.44
CSp0.05	7.48	7.92	7.51	7.29	7.39	6.30	CSh0.05	7.44	7.93	7.51	7.38	7.58	6.67
HSp0.05	7.44	7.95	7.56	7.37	7.49	6.51	HSh0.05	7.44	7.94	7.53	7.38	7.57	6.63
FSp0.05	7.15	8.12	7.77	7.73	7.91	7.48	FSh0.05	7.21	8.09	7.74	7.69	7.93	7.49
$ \Delta $	0.33	0.20	0.26	0.44	0.52	1.18	$ \Delta $	0.23	0.16	0.23	0.31	0.36	0.86
$\langle \Delta \rangle$	0.18	0.15	0.24	0.47	0.41	0.47	$\langle \Delta \rangle$	0.12	0.11	0.18	0.32	0.23	0.45

the correlation; however, as pointed out by Stasińska (2005), at high metallicities, the temperature derived from the [O II] line ratio may be strongly in error due to the contribution of recombination from O⁺⁺.

3.4 Abundance diagnostics

We have assessed that the geometrical distribution of stars within a H II region plays a role in the temperature structure of the gas, the magnitude of these effects will clearly be dependent on the total mass of the stars and the concentration level. It is important now to verify the robustness of commonly used metallicity indicator against these temperature shifts. In particular, we are interested in identifying systematic trends with stellar distribution rather than absolute errors. Table 4 lists the *empirical* oxygen abundances obtained using six different indicators. We used the following calibrations for the six indicators: (1) O₂₃ – Pilyugin (2000, 2001b), (2) O₃N₂ – Stasińska (2006), (3) N₂ – Pettini & Pagel (2004), (4) S₂₃ – Pérez-Montero & Díaz (2005), (5) S₃O₃ – Stasińska (2006) and (6) Ar₃O₃ – Stasińska (2006). It is worth reiterating at this point that metallicity indicators should, and generally are, only be used for statistical studies as the error on a single region may be very large; the models presented in this work do not attempt to cover the full parameter space occupied by H II regions and therefore do not aim at identifying the most accurate indicator *in absolute terms*. Here, we are mainly interested in studying a possible systematic error in the derived abundances introduced by the 3D stellar distribution. For this reason for each trio of models (C, H and F for a given density distribution and metallicity), we compute Δ , the largest difference between the oxygen abundance in log units derived from Cases C, H and F.

The results are summarized in Table 4, where the mean values $\langle \Delta \rangle$ are also listed. For all metallicity indicators apart from O₂₃, there is a

clear trend for higher metallicity being derived from models ionized by fully distributed sources, Case F, than from Case C and H models. The reverse is true for O₂₃, where metallicities derived from Case F models are smaller than those derived from Case C and H models. The Δ values at a given metallicity vary from one indicator to the next; however they are rarely below ~ 0.1 dex (only for the highest metallicity case), with more representative values around 0.3 dex for the spherical case, but often larger than 0.4 (and larger than 1.1 dex in one case). These deviations are slightly smaller for the shell density distributions; this is obvious as even for F cases most of the ionizing radiation in these models will be emitted from the central cavity, reducing the differences between C and F cases. We note that in some cases the values given by the Case H models are lower than those given by the respective Case C models (rather than being equal or in the middle between C and F). We have analysed these deviations statistically and can confirm that the small differences are simply due to the variance of our Monte Carlo models and do not bear any physical significance.

The reason for the systematic effect we see in the *empirical* abundance determinations can be understood by re-examining Fig. 3, where the ionization sequence of our model is parametrized in terms of oxygen and sulphur emission lines. The C (small symbols), H (medium symbols) and F (large symbols) form a sequence, with the Case F models generally showing a lower ionization parameter than Case C and H models. The differences in the abundances derived from Cases C to F with the various indicators clearly reflect the different dependence of each indicator on the ionization parameter. This can be simply shown for an idealized system. The ionization parameter of a pure-hydrogen spherical volume of gas with number density N_{H} ionized by a source emitting $Q_{\text{H}\beta}$ hydrogen-ionizing photons per second is defined as $U = Q_{\text{H}\beta} / (4\pi N_{\text{H}} R_s^2)$, where R_s is the Strömgen radius. In such a system, from the ionization balance

equation (e.g. Osterbrock 1989, equation 2.19) R_s is directly proportional to $Q_{\text{H}0}^{1/3}$ and to $N_{\text{H}}^{-2/3}$, neglecting the temperature dependence of the hydrogen recombination coefficient. For simplicity, we compare the ionization parameter of the system above, U^C , ionized by only one source, to that of a similar system (F) ionized by N_s identical sources each emitting $Q_{\text{H}0}/N_s$ hydrogen-ionizing photons per second. With these assumptions, it is easy to show that the ionization parameter, U^F , for system F, measured at the Strömgren radius of each individual source, is simply related to U^C by

$$U^F = U^C N_s^{-1/3} \quad (2)$$

and therefore always smaller than U^C for $N_s > 1$.

The magnitude of the errors in the metallicity derived by the strong line methods is significant. It is, however, true that the effects reported here represent a worst case scenario, and our extreme assumptions on stellar populations create a large dispersion in the resulting ionization parameters, which in some cases exceeds the observed range, as seen in Figs 2 and 3. Aside from the magnitude of the Δ values, however, a worrying aspect is the fact that the discrepancies between Cases C, H and F are systematic. This can have an impact on galactic metallicity gradients determined via strong line methods, if these are calibrated via photoionization models. In fact, if compact clusters (close to Case C) and loose associations (close to Case F) are randomly distributed throughout a given galaxy, then the systematic errors would only cause a larger scatter in the observed metallicities, but, given sufficient number statistics, they would not affect the measured metallicity gradient. However, if the ratios of compact clusters to loose associations are somewhat dependent on the galactocentric distance, then the systematic errors due to stellar geometrical distributions may indeed introduce a bias on the measured galactic metallicity gradient, if the abundances are obtained from strong line methods calibrated on ab initio models which do not reproduce the observed excitation of H II regions. For example, recent work by Rosolowsky et al. (2007), presenting high-resolution molecular gas maps of M33, showed a truncation in the mass distribution of giant molecular clouds (GMCs) at a galactocentric distance of 4 kpc. A recent study on the demographics of young star-forming clusters in M33 by Bastian et al. (2007) also shows the same cut-off at 4 kpc for the clusters detected. We could interpret this as tentative evidence of different star formation environments from the centre to the edge of M33, however, we prefer to postpone this discussion until more compelling observational evidence becomes available.

4 CONCLUSIONS

Following our theoretical investigation on the effects of the spatial configuration of ionization sources on the temperature structure of H II regions, we summarize our conclusions as follows:

(i) For intermediate to high metallicities ($0.4 \leq Z/Z_{\odot} \leq 2$), for a given gas density distribution, abundance and ionizing spectral shape and intensity, a model with a central concentration of stars (Case C) will result in higher ionic temperatures for high-ionization species (O^{2+} , S^{2+} , etc.), compared to the same model with stars fully distributed within the volume (Case F). The opposite is true for ‘low’ ionization species (e.g. O^+ , N^+). This results in shallower gradients in the electron temperature distribution across the ionic species zones.

(ii) Low-metallicity models ($Z/Z_{\odot} \leq 0.2$) do not show the temperature inversion from low to high ionic species zones, rather a

shift in the temperature is experienced by all ionic species zones, resulting in Case F models being cooler than Case C and H models.

(iii) At intermediate to high metallicity ($Z/Z_{\odot} \geq 0.4$), models with stars distributed within the full volume are more isothermal (show lower t^2 values) than the same models with a central concentration of stars. These temperature ‘fluctuations’ obtained for Case C models are a simple consequence of a large temperature gradient. Multiple ionizing sources of different temperatures at central or non-central locations do not produce significant temperature fluctuations in the ionized gas of models with $Z/Z_{\odot} \geq 0.4$.

(iv) At low metallicities ($Z/Z_{\odot} \leq 0.2$), models with stars distributed within the full volume (Case F) show *larger* t^2 values than the same models with a central concentration of stars. Here, we are seeing the effects of true temperature ‘fluctuations’ for Case F models. The magnitude of $t^2(\text{O}^{2+})$ remains, however, too small to have any significant effect on derived abundances.

(v) Multiple ionizing sources of different temperatures at central or non-central locations are not the cause of significant temperature fluctuations in the ionized gas of our models with $0.05 \leq Z/Z_{\odot} \leq 2$.

(vi) The relation $t^2(\text{O}^+) = t^2(\text{O}^{2+})$, often used in empirical studies, is *not* verified by our models. Extreme care should be taken to account for the uncertainties introduced by the use of this relation in studies seeking to apply corrections to CEL-derived abundances making use of an empirical estimation of temperature fluctuations. For our $Z/Z_{\odot} = 2$ models, $t^2(\text{O}^{2+})$ is always a factor of 2 or more higher than $t^2(\text{O}^+)$, while for lower metallicities $t^2(\text{O}^{2+})$ becomes lower than $t^2(\text{O}^+)$ sometimes by large factors (up to approximately 10).

(vii) For intermediate- to high-metallicity models, electron temperatures in the O^{2+} and O^+ ionization zones are shifted in opposite directions, contributing to the scatter observed in the $T_e(\text{O}^{2+})$ versus $T_e(\text{O}^+)$ relation. We confirm that H II region abundances derived on the basis of the $T_e(\text{O II})$ alone should, therefore, be considered highly uncertain.

(viii) Metallicity indicators calibrated by grids of spherically symmetric photoionization models may suffer a systematic bias due to their dependence on the ionization parameter of the system. For the same input parameters, Case F models will always result in smaller ionization parameters than Case C and H models. The errors estimated in this work (typically 0.3 dex, but larger in some cases) are likely to represent the worst-case scenario, but nevertheless their magnitude and their systematic nature do not allow them to be ignored.

ACKNOWLEDGMENTS

BE would like to thank the organizers, Fabio Bresolin and Lisa Kewley, and all the participants of the Metals07 workshop on Metallicity Calibrations for Gaseous Nebulae (held at the Institute for Astronomy of the University of Hawaii on 2007 January 22–26) for productive discussion and advice for this work. We would also like to thank Rob Kennicutt for his many suggestions and Christophe Morisset and Luc Jamet for their comments and for their careful study of our results. BE was partially supported by *Chandra* grants GO6-7008X and GO6-7009X. NB was supported by a PPARC Postdoctoral Fellowship. NB gratefully acknowledges the hospitality of the Harvard-Smithsonian Centre for Astrophysics, where a significant part of this work took place. The authors wish to thank the referee, Jorge García-Rojas, for helpful comments and constructive discussion.

REFERENCES

- Allende Prieto C., Lambert D. L., Asplund M., 2001, *ApJ*, 556, L63
- Allende Prieto C., Lambert D. L., Asplund M., 2002, *ApJ*, 573, L137
- Alloin D., Collin-Souffrin S., Joly M., Vigroux L., 1979, *A&A*, 78, 200
- Bastian N., Ercolano B., Gieles M., Rosolowsky E., Scheepmaker R., Gutermuth R., Efremov Y. 2007, *MNRAS*, in press (doi:10.1111/j.1365-2966.2007.12064.x) (arXiv:0706.0495)
- Bresolin F., Kennicutt R. C., Garnett D. R., 1999, *ApJ*, 510, 104
- Bresolin F., Garnett D. R., Kennicutt R. C., 2004, *ApJ*, 615, 228
- Bresolin F., Schaerer D., González Delgado R. M., Stasińska G., 2005, *A&A*, 441, 981
- Charlot S., Longhetti M., 2001, *MNRAS*, 323, 887
- Ercolano B., Storey P. J., 2006, *MNRAS*, 372, 1875
- Ercolano B., Barlow M. J., Storey P. J., Liu X.-W., 2003a, *MNRAS*, 340, 1136
- Ercolano B., Morisset C., Barlow M. J., Storey P. J., Liu X.-W., 2003b, *MNRAS*, 340, 1153
- Ercolano B., Barlow M. J., Storey P. J., Liu X.-W., Rauch, T., Werner K., 2003c, *MNRAS*, 344, 1145
- Ercolano B., Barlow M. J., Storey P. J., 2005, *MNRAS*, 362, 1038
- Esteban C., Peimbert M., García-Rojas J., Ruiz M. T., Peimbert A., Rodríguez M., 2004, *MNRAS*, 355, 229
- García-Rojas J., Esteban C., Peimbert M., Rodríguez M., Ruiz M. T., Peimbert A., 2004, *ApJS*, 153, 501
- García-Rojas J., Esteban C., Peimbert A., Peimbert M., Rodríguez M., Ruiz M. T., 2005, *MNRAS*, 362, 301
- García-Rojas J., Esteban C., Peimbert M., Costado M. T., Rodríguez M., Peimbert A., Ruiz M. T., 2006, *MNRAS*, 368, 253
- García-Rojas J., Esteban C., Peimbert A., Rodríguez M., Peimbert M., Ruiz M. T., 2007, *Rev. Mex. Astron. Astrofis.* 43, 3
- Garnett D. R., 1992, *AJ*, 103, 1330
- Garnett D. R., Kennicutt R. C., Jr, 1994, *ApJ*, 426, 123
- Garnett D. R., Shields G. A., Skillman E. D., Sagan S. P., Dufour R. J., 1997, *ApJ*, 489, 63
- Grevesse N., Sauval A. J., 1998, *Space Sci. Rev.*, 85, 161
- Hägele G. F., Pérez-Montero E., Díaz Á. I., Terlevich E., Terlevich R., 2006, *MNRAS*, 372, 293
- Holweger H., 2001, in Wimmer-Schweingruber R. F., ed., *AIP Conf. Proc. Vol. 598, Joint SOHO/ACE Workshop 'Solar and Galactic Composition'*. Am. Inst. Phys., New York, p. 23
- Izotov Y. I., Stasińska G., Meynet G., Guseva N. G., Thuan T. X., 2006, *A&A*, 448, 955
- Landi E., Dere K. P., Young P. R., del Zanna G., Mason H. E., Landini M., 2005, in Smith R. K., ed., *AIP Conf. Proc. Vol. 774, X-Ray Diagnostics of Astrophysical Plasmas: Theory, Experiment, and Observation*. Am. Inst. Phys., New York, p. 409
- Kennicutt R. C., Jr, 1996, *ApJ*, 456, 504
- Kennicutt R. C., Bresolin F., Garnett D. R., 2003, *ApJ*, 591, 801
- Kewley L. J., Dopita M. A., 2002, *ApJS*, 142, 35
- Kingdon J., Ferland G. J., 1995, *ApJ*, 442, 714
- Leitherer C. et al., 1999, *ApJS*, 123, 3
- Liu X.-W., Barlow M. J., Zhang Y., Bastin R., Storey P. J., 2006, *MNRAS*, 368, 1959
- Lodders K., 2003, *ApJ*, 591, 1220
- McCall M. L., Rybski P. M., Shields G. A., 1985, *ApJS*, 57, 1
- McGaugh S. S., 1991, *ApJ*, 380, 140
- Osterbrock D. E., 1989, Research supported by the University of California, John Simon Guggenheim Memorial Foundation, University of Minnesota, et al. Mill Valley, CA, University Science Books, p. 422
- Osterbrock D. E., Tran H. D., Veilleux S., 1992, *ApJ*, 389, 196
- Pagel B. E. J., Edmunds M. G., Blackwell D. E., Chun M. S., Smith G., 1979, *MNRAS*, 189, 95
- Peimbert M., 1967, *ApJ*, 150, 825
- Peimbert M., 1971, *Bol. Obs. Tonantzínla Tacubaya*, 6, 29
- Peimbert A., 2003, *ApJ*, 684, 735
- Peimbert M., Costero R., 1969, *Bol. Obs. Tonantzínla Tacubaya*, 5, 3
- Peimbert M., Peimbert A., 2003, *Rev. Mex. Astron. Astrofis.*, 16, 113
- Peimbert M., Peimbert A., 2006, in Barlow M. J., Mendez R. H., eds, *Proc IAU Symp. 234, Planetary Nebulae in our Galaxy and Beyond*. Cambridge Univ. Press, Cambridge, p. 227
- Peimbert M., Peimbert A., Ruiz M. T., 2000, *ApJ*, 541, 688
- Peimbert A., Peimbert M., Ruiz M. T., 2005, *ApJ*, 634, 1056
- Pérez-Montero E., Díaz A. I., 2003, *MNRAS*, 346, 105
- Pérez-Montero E., Díaz A. I., 2005, *MNRAS*, 361, 1063
- Pettini M., Pagel B. E. J., 2004, *MNRAS*, 348, L59
- Pilyugin L. S., 2001a, *A&A*, 373, 56
- Pilyugin L. S., 2001b, *A&A*, 369, 594
- Pilyugin L. S., 2000, *A&A*, 362, 325
- Rosolowsky E., Keto E., Matsushita S., Willner S., 2007, *ApJ*, 661, 830
- Roy J.-R., Walsh J. R., 1997, *MNRAS*, 288, 715
- Rubin R. H. et al., 2002, *MNRAS*, 334, 777
- Smith L. J., Norris R. P. F., Crowther P. A., 2002, *MNRAS*, 337, 1309
- Stasińska G., 1980, *A&A*, 85, 359
- Stasińska G., 1982, *A&AS*, 48, 299
- Stasińska G., 2005, *A&A*, 434, 507
- Stasińska G., 2006, *A&A*, 454, L127
- Storchi-Bergmann T., Calzetti D., Kinney A. L., 1994, *ApJ*, 429, 572
- Tsamis Y. G., Péquignot D., 2005, *A&A*, 364, 687
- Tsamis Y. G., Barlow M. J., Liu X.-W., Danziger I. J., Storey P. J., 2003, *MNRAS*, 338, 687
- van Zee L., Salzer J. J., Haynes M. P., O'Donoghue A. A., Balonek T. J., 1998, *AJ*, 116, 2805
- Veilleux S., Osterbrock D. E., 1987, *ApJS*, 88, 295
- Vilchez J. M., Esteban C., 1996, *MNRAS*, 280, 720
- Walsh J. R., Roy J.-R., 1997, *MNRAS*, 288, 726
- Wesson R., Liu X.-W., Barlow M. J., 2005, *MNRAS*, 362, 425
- Zhang Y., Ercolano B., Liu X.-W., 2007, *A&A*, 464, 631

This paper has been typeset from a $\text{\TeX}/\text{\LaTeX}$ file prepared by the author.